



Complex impedance and electric modulus of flexible ferroelectric polymer PVDF-ZnO hybrid nanocomposite thin films

A. H. Arshad¹ · Santhoshkumar Dani¹ · Bibi Raza Khanam¹ · Ramcharan Meena² · V. Jagadeesha Angadi³ · Udaykumar V. Khadke¹

Received: 26 September 2023 / Revised: 20 March 2024 / Accepted: 6 May 2024 /
Published online: 23 May 2024

© The Author(s), under exclusive licence to Springer-Verlag GmbH Germany, part of Springer Nature 2024

Abstract

Ferroelectric polymer-based separators, known for their flexibility, ease of synthesis, and modifiability through dopants, are currently under extensive study due to their potential applications in electronic devices. PVDF nanocomposites, which combine the strengths of their constituents, currently lead in emerging technologies. This research employs Zinc oxide nanoparticles (ZnO NPs) as fillers in the PVDF matrix and investigates their structural, optical, thermal and electrical properties. ZnO NPs synthesized via the combustion method, are being incorporated with varying concentrations (2, 4, 6, 8, and 10 wt%), into PVDF nanocomposite (PNC) thin films through a solution casting process. The PNC thin films are characterized using XRD, FTIR, UV–Vis spectroscopy and thermogravimetric analysis (TGA). Dielectric properties are being explored across a frequency range from 20 to 2 MHz at room temperature, revealing enhanced dielectric constants at lower frequencies, decreasing with frequency due to Maxwell–Wagner interfacial polarization. With increasing frequency, AC conductivity and electric modulus exhibit enhancement. Complex impedance analysis via the Cole–Cole plot indicates a non-Debye type of dielectric relaxation with heightened conductivity. TGA demonstrates improved thermal stability in PNC thin films. These findings suggest the potential application of the prepared PNC thin films as separators in energy storage devices.

Keywords PVDF nanocomposites · Dielectric properties · AC conductivity · Modulus · Cole–Cole plot

✉ Udaykumar V. Khadke
khadke@vskub.ac.in

¹ Department of Physics, Vijayanagara Sri Krishnadevaraya University, Ballari 583105, India

² Inter University Accelerator Centre, Aruna Asaf Ali Marg, New Delhi 110067, India

³ Department of Physics, P.C. Jabin Science College, Hubballi, Karnataka 580031, India

Introduction

Batteries are the portable energy storage devices that convert chemical energy into electrical energy, find widespread use across numerous applications, including smart phones, laptops, tablets, aerospace, aviation, space satellites, electric vehicles (EVs), medical devices, and marine applications. Various battery types are available, with efficiency and lifespan determined by the materials used. Lithium-ion batteries (LIBs) are prominent for their extended discharge capability, high energy density, and eco-friendliness [1, 2]. Nevertheless, challenges like long charging times, dendrite formation, short circuit risks, limited lifespan, cycle counts, and temperature-induced degradation persist. The electrodes and separators within batteries are pivotal in enhancing efficiency and longevity. These issues can be mitigated through the development of efficient polymer-based separators.

Polymer batteries are a versatile class of rechargeable energy storage solutions that employ a polymer electrolyte, offering flexibility, lightweight design, a high energy density, noted for their rapid charging capabilities, sustained at wide temperature ranges, and customizable shapes. Considered safer alternatives with built-in protection circuitry, polymer batteries have gained prominence in modern gadgets particularly in electric vehicles, delivering an attractive blend of performance and adaptability. On the other hand, PVDF batteries, featuring polyvinylidene fluoride in their construction, are advanced energy storage systems known for their superior safety and performance. PVDF plays a critical role in preventing short circuits as the separator component of lithium-ion and lithium-polymer batteries, offering high electrochemical stability, heat resistance, and chemical resistance, enhancing battery reliability, ion transport, and customizable properties, PVDF separators are instrumental in various applications, from consumer electronics to electric vehicles and energy storage systems [3, 4].

PVDF is used as a separator in the battery, due to the presence of a high electron withdrawing functional group (-C-F-) combination and its high dielectric constant confirms the higher degree of electrochemical stability, which increases the moment of charge carriers [5]. The huge flexibility, mechanical strength, and thermal sustainability of the PVDF make it a suitable material in field of electronics, sensors, energy storage devices, etc. PVDF, a semi-crystalline ferroelectric polymer composed of $-\text{CH}_2\text{-CF}_2$ monomers, exhibits mainly in α (pseudo-orthorhombic), β (orthorhombic), and γ (monoclinic) crystalline forms based on crystallization conditions and chain conformations. These forms are characterized by trans-(T) or gauche (G) linkages of VDF monomers: TGTGTG, TTTT, and TTTGTTTG, respectively. β -phase is the most commonly used phase due to a robust fluorine and hydrogen polar bond, boasting the highest dipole moment (7×10^{-30} C·m), [6, 7]. The pure PVDF shows limitation, such as thermal degradation, limited binding strength due to lack of chemical bonds, low electronic and lithium-ion conductivities, and these shortcomings can be overcome by doping with the inorganic metal oxides in the PVDF matrix [4]. Doping the nano-metal oxides in PVDF polymer matrix improves the dielectric properties, and can easily

design the NC thin films as separator in battery design [8, 9]. Recently, the ZnO NPs attracted great attention as fillers for preparation of polymer NCs. In recent reports, it is observed that the incorporation of ZnO NPs in the polymer matrix increases the electrical and optical properties of polymers because of strong interfacial interaction between the organic–inorganic NPs [10, 11].

In this paper, we are reporting the synthesis, characterization and the complex impedance, and electric modulus measurements of PVDF thin films incorporated with ZnO NP in PVDF polymer matrix for application in energy storage devices with emphasize its thermal and dielectric studies.

Materials and methods

Polyvinylidene fluoride (PVDF) ($M_w = 534,000$) was obtained from Sigma Aldrich, India; whereas, N–N–dimethylacetamide (DMAC), ZnO ($M_w = 81.39$, AR grade, purity 99.9%), and Urea ($M_w = 60.06$, purity 99%), were procured from SD-Fine Chem. Ltd. Mumbai, India. These chemicals were used for the synthesis of ZnO NPs and also in the preparation of PVDF and PNC thin films using the solution casting technique. To minimize errors, we use calibrated equipment and conduct experiments in a clean and laminar airflow platform under ambient laboratory conditions.

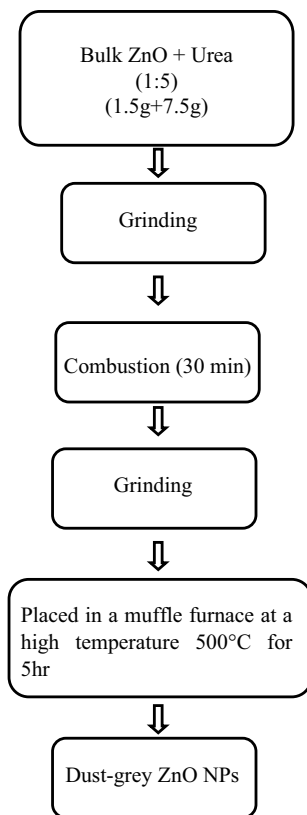
Synthesis of ZnO nanoparticles

ZnO NPs were prepared by chemical combustion method using urea as a fuel. Bulk ZnO (1.5 gm) is grounded with urea (7.5 gm) making sure 1:5 ratio of the precursor and fuel. This mixture was then subjected to a combustion process for 30 min under an oxidizing agent. Thus, the obtained precursor was ground again for 30 min and subsequently placed in a muffle furnace at a high temperature (500 °C) for 5 h to obtain dust-gray ZnO NPs. Figure 1 depicts the sequential process flow chart involved in the combustion method for the preparation of ZnO NPs [12].

Preparation of PVDF and PNC thin films

Figure 2 illustrates the process of preparing pristine PVDF and PNC thin films using the solution casting method using thin film applicator. Initially, a specific quantity of PVDF was dissolved in 15 mL of DMAC with continuous stirring on a magnetic stirrer for 5 h. Subsequently, 2 wt% of ZnO NPs were introduced into the clear dissolved solution while stirring continuously, and the mixture was stirred for an additional 2 h. Furthermore, the homogeneous dispersion of ZnO NPs was achieved through Ultrasonic Sonication for 20 min to ensure better distribution of NPs in the PVDF matrix. The resulting PNC solution was then cast onto a glass sheet using a doctor blade. Thereafter, the glass sheet was immersed in a distilled water bath maintained at 4–6 °C to facilitate phase inversion, and the film was carefully peeled off and named as PNC2. It was allowed to dry in a hot air oven at a temperature of 50 ± 2 °C for 3 h to remove the moisture. The same procedure was repeated for 4, 6,

Fig. 1 Flowchart representing the procedure of ZnO NP synthesis using the combustion method



8, and 10 wt% of ZnO NPs [13] and labeled as PNC4, PNC6, PNC8, and PNC10, respectively. The sample codes, descriptions, and thicknesses of the prepared PVDF and PNCs thin films are presented in Table 1. Film thickness measurements were conducted using a digital gauge meter with an accuracy of $\pm 10 \mu\text{m}$. The variations in peak intensity at 2θ values obtained from the XRD pattern are reported in Table 2.

Characterization and measurement

To determine the crystalline nature and average crystallite size of the prepared nanocomposite thin films, X-ray diffraction (XRD) patterns were recorded using an X-ray diffractometer (XRD-Rigaku Miniflex, Japan) with 2θ intervals ranging from 10° to 90° . X-rays ($\lambda = 0.154 \text{ nm}$) were detected using a DteX250H detector, operated at 40 kV and 30 mA, with a $\text{CuK}\alpha$ 1D filter. Fourier transform infrared spectra were obtained using FTIR spectroscopy (PerkinElmer Spectrum Two L160000U, USA) in the wavenumber range of 400 cm^{-1} to 4000 cm^{-1} . Optical properties were investigated using a UV–Vis spectrometer (PerkinElmer Instruments Lambda 900) in the wavelength range of 200 to 800 nm. Thermo-gravimetric analysis (TGA) measurements (PerkinElmer STA 8000)

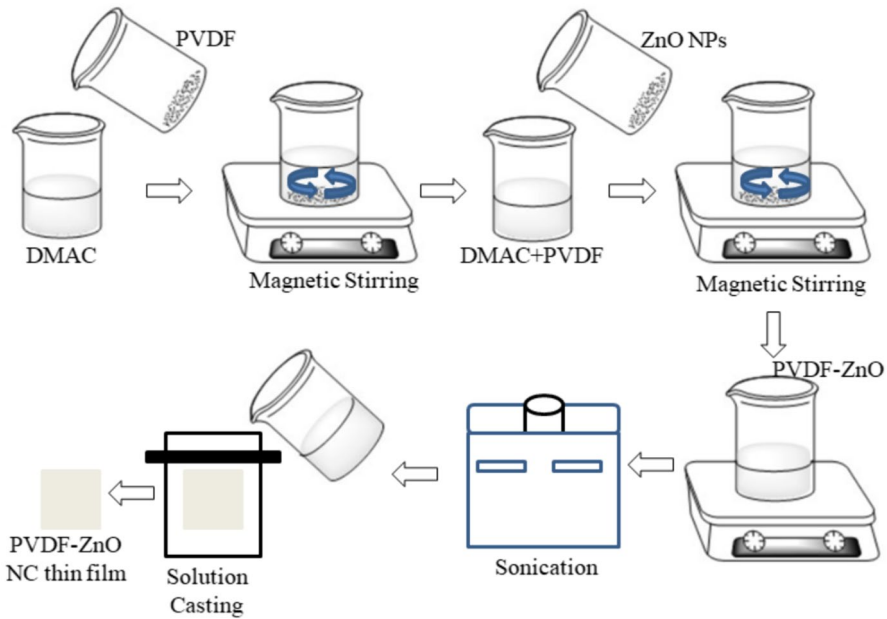


Fig. 2 Film casting technique used to prepare the PNC thin films

Table 1 Sample codes and descriptions, with film thickness for PVDF and PNC thin films

Sample code	Sample description	Thickness (μm)
Pristine PVDF	PVDF without ZnO NP doping	230 ± 18
PNC2	PVDF with 2 wt% ZnO NP	160 ± 15
PNC4	PVDF with 4 wt% ZnO NP	130 ± 12
PNC6	PVDF with 6 wt% ZnO NP	120 ± 10
PNC8	PVDF with 8 wt% ZnO NP	180 ± 16
PNC10	PVDF with 10 wt% ZnO NP	160 ± 15
ZnO NPs	Zinc oxide nanoparticles	–

were performed under a nitrogen atmosphere, with a temperature range from 30 to 800 °C and a heating rate of 20 °C/min. Dielectric studies, AC conductivity of the nanocomposite thin films, were examined using an LCR meter (Agilent E4980A, USA) over a frequency range from 20 to 2 MHz at room temperature. Film surfaces were Au-coated using vacuum evaporation for electrodes to study dielectric properties. Graphs were plotted and analyzed using Origin software 8.5 (2019b). Further XRD analysis was conducted using Expert Highscore software; while, Z-view software was used for Cole–Cole plots.

Table 2 Details of film thickness and variation of intensity of PVDF, PNCs and ZnO samples in XRD pattern

Sample code	Thickness in μm	Intensity at angle				
		$2\theta = 18.3^\circ$	$2\theta = 20.4^\circ$	$2\theta = 31.72^\circ$	$2\theta = 34.39^\circ$	$2\theta = 36.2^\circ$
Pristine PVDF	230 ± 11	86.273	112.63	–	–	–
PNC2	160 ± 8	86.273	12616.67	4150.00	6916.66	6000.00
PNC4	130 ± 6	–	8500.00	7116.66	10678.16	11100.00
PNC6	120 ± 6	12349.45	17298.57	10509.97	12018.63	14867.47
PNC8	180 ± 9	12375.54	15610.98	12852.18	12018.63	17754.36
PNC10	160 ± 8	–	9183.33	12283.33	13300.00	19300.00
ZnO NPs	–	–	–	13783.33	12383.33	18241.67

Results and discussion

X-ray diffraction analysis

Figure 3 depicts the XRD patterns of pristine PVDF, as synthesized ZnO NPs, and polymer nanocomposites (PNC2, PNC4, PNC6, PNC8, and PNC10). The XRD analysis of the pristine PVDF film reveals peaks at 18.3° and 20.5° , confirming the presence of α and β phases of PVDF with crystal planes (2 0 2) and (1 1 0), respectively. The relatively high intensity peak at 20.5° indicates the dominance of the β phase, with lattice constants estimated to be $a = 4.9700 \text{ \AA}$, $b = 9.6700 \text{ \AA}$, and $c = 9.2400 \text{ \AA}$, in good agreement with the literature [14, 15].

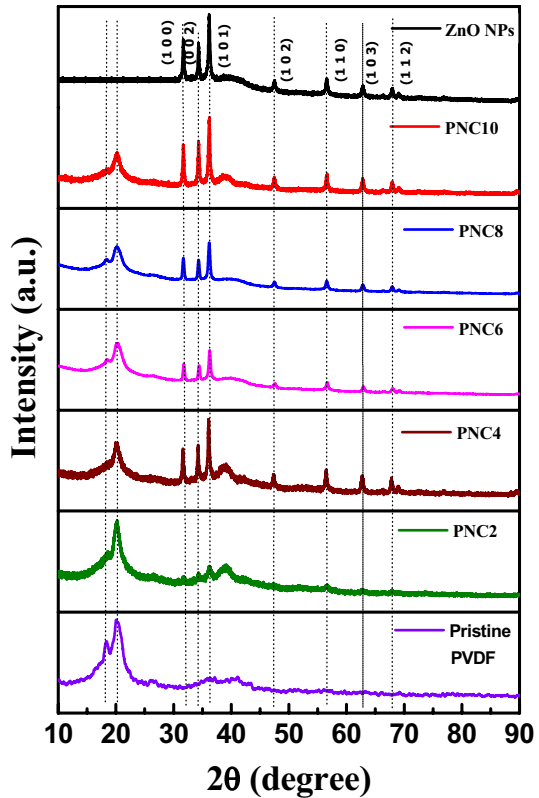
The XRD pattern of synthesized ZnO NPs in Fig. 3 reveals peaks at 31.62° , 34.35° , 36.18° , 47.25° , 56.35° , 62.73° , and 68.04° , corresponding to crystal planes (1 0 0), (0 0 2), (1 0 1), (1 0 2), (1 1 0), (1 0 3), (1 1 2), and (2 0 1), respectively, with lattice constants $a = 3.2530 \text{ \AA}$, $b = 3.2530 \text{ \AA}$, and $c = 5.2130 \text{ \AA}$, confirming the presence of the hexagonal wurtzite structure of ZnO NPs (JCPDS No. 01–076-0704). The sharp and intense peaks confirm the high degree of crystallinity of the ZnO NPs. In contrast, the β phase ($\sim 70\%$) dominates over the α phase ($\sim 30\%$) in pure PVDF and in all PNCs, as indicated by their relative intensities, without altering the structure of the ZnO NPs in the PVDF matrix. The average crystallite size (D_{hkl}) of ZnO NPs is found to be 15.66 nm, 15.60 nm, 26.59 nm, 26.30 nm, 25.47 nm, and 28.50 nm in pure ZnO NPs, PNC2, PNC4, PNC6, PNC8, and PNC10, respectively, calculated using the Debye–Scherrer (D-S) formula (Eq. 1) [16, 17].

$$D_{hkl} = \frac{K\lambda}{\beta_{hkl}\cos\theta} \quad (1)$$

where K —particle shape factor = 0.9, λ —wavelength of the X-ray in nm— β_{hkl} half width full maxima in radian, and θ —Bragg's angle in radian.

Williamson's and Strain–strain formulae establishes mathematical relationships between diffraction peak broadening, crystallite size, lattice strain, and related factors, is given by Eq. (2) and (3), respectively,

Fig. 3 XRD plots of ZnO NPs and composites PNC2, PNC4, PNC6, PNC8, and PNC10



$$\varepsilon = (\beta) / (4 \tan \theta) \tag{2}$$

$$(d_{hkl}\beta_{hkl} \cos \theta)^2 = \frac{k}{D} (d_{hkl}^2 \beta_{hkl} \cos \theta) + \left(\frac{\varepsilon}{2}\right)^2 \tag{3}$$

where ε —lattice strain, θ —Bragg’s angle in radian, and β_{hkl} half width full maxima in radian.

Size–strain plots visually illustrate the relationship between crystallite size and micro-strain, providing insights into how lattice strain affects crystallite size by taking $(d_{hkl}^2 \beta_{hkl} \cos \theta)^2$ and $(d_{hkl} \beta_{hkl} \cos \theta)^2$ were taken on x-axis and y-axis, respectively. The strain and particle size were determined from the slope and y-intercept of the fitted line, respectively. The average crystallite sizes were also estimated through modified D-S, Williamson–Hall (W–H), and size–strain (S–S) plots for all samples, as shown in Fig. 4a, b, and c, respectively. They were compared with those obtained from the D–S method for all samples and found to be identical, indicating confirmation of the crystallite sizes of ZnO NPs. The degree of crystallinity enhanced as the wt% of ZnO NPs increased in the PVDF matrix and the same is tabulated in Table 3.

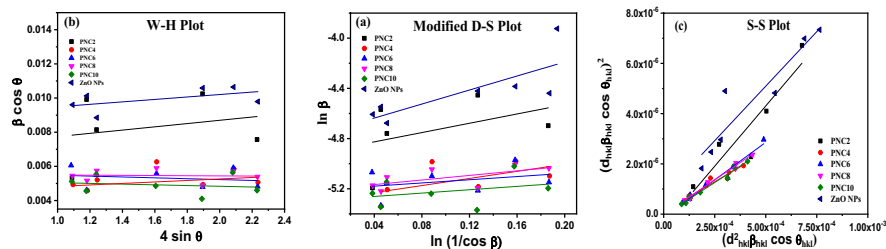


Fig. 4 Modified D–S, W–H, S–S plots of ZnO NPs and composites PNC2, PNC4, PNC6, PNC8, and PNC10

Table 3 The crystallite size of ZnO NPs estimated using Debye–Scherrer formula, modified Debye–Scherrer (D–S), Williamson–Hall (W–H), stress–strain (S–S) plots and % degree of crystallinity

Sample code	Average crystallite size (nm)				Degree of crystallinity (%)
	D-S Formula	Modified D–S plot	W–H plot	S–S plot	
ZnO NPs	15.66	15.98	15.78	15.97	–
PVDF	–	–	–	–	18
PNC2	15.60	14.99	15.40	18.30	21
PNC4	26.59	27.41	23.49	29.19	22
PNC6	26.30	25.22	24.15	23.17	23
PNC8	25.47	25.19	24.97	25.29	26
PNC10	28.50	27.43	26.35	26.25	27

However, the average crystallite size of ZnO nanoparticles in the PVDF matrix increases and remains saturated with an increase in the wt% of ZnO NPs. This is attributed to the capping of ZnO nanoparticles by the PVDF matrix. Conversely, a linear increase in the peak intensities of ZnO NPs is observed with an increase in the wt% of ZnO NPs in the PVDF polymer, indicating the retained crystalline nature of the NPs. In the $30 < 2\theta < 70$ region, it is noteworthy that the diffraction peaks of ZnO NPs affirm the homogeneous dispersion of ZnO NPs within the PVDF matrix [18].

FTIR spectra analysis

Figure 5 displays the FTIR spectra of prepared PNC2 to PNC10 thin films. The peaks at 3025 cm^{-1} and 2985 cm^{-1} confirm the strong absorption bands corresponding to the symmetric stretching and asymmetric vibrations of the CH_2 group in PVDF. The flat, continuous absorption band observed between 1450 cm^{-1} and 1000 cm^{-1} represents fluorocarbon absorption (C–F). The peak at 544 cm^{-1} confirms the stretching vibration modes of Zn–O–Zn in all PNCs. The vibrational bands at 760 cm^{-1} , and 980 cm^{-1} shows the presence of α -phase in PVDF and in some of the PNC films, the peaks at 613 cm^{-1} , 757 cm^{-1} , 975 cm^{-1} align well with

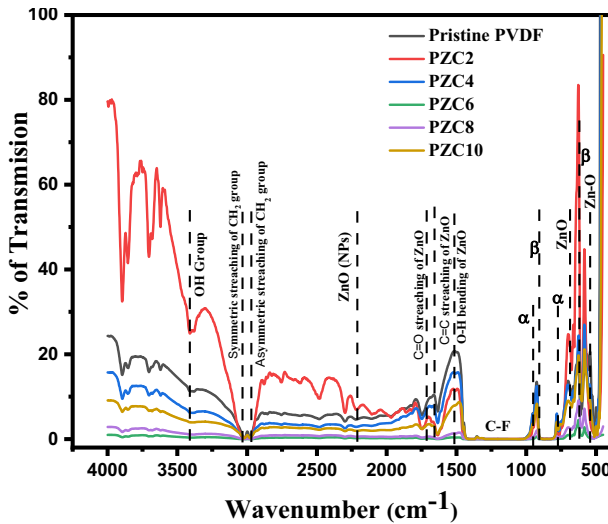


Fig. 5 FT-IR spectra of pristine PVDF and PNC2, PNC4, PNC6, PNC8, and PNC10 thin films

previously reported values, indicating that PVDF in the PNC films exists in the β-phase, also confirmed by X-ray diffraction analysis [19, 20].

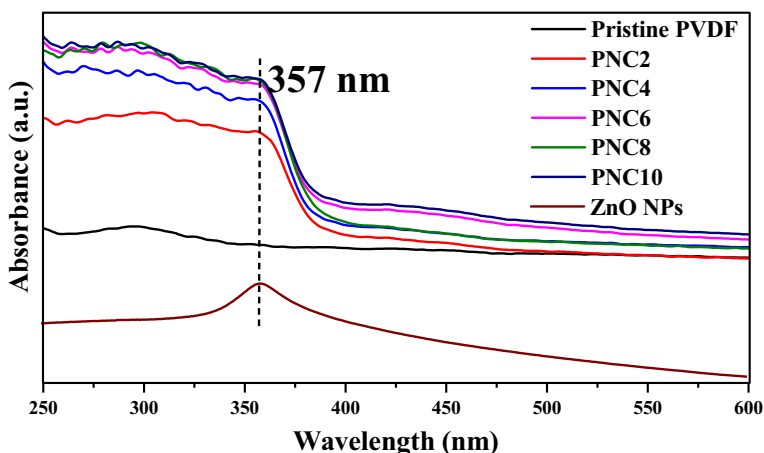
Additionally The double bond C=O mode exhibits symmetric vibrations around 1700 cm⁻¹. Peaks observed at 1600 cm⁻¹ and 1500 cm⁻¹ correspond to C=C stretch, O–H bending of the ZnO NPs, respectively. The spectra of the PNCs exhibit slight shifts toward longer wave numbers due to the formation of hydrogen bonds between the oxygen of ZnO and the hydrogen of the –CH-group present in the polymer [13, 18]. Phase separation between PVDF and ZnO creates distinct areas with varied chemical compositions, impacting FTIR transmission. Varied interaction strengths at different interfaces within the composite contribute to non-sequential transmission. Additionally, ZnO-induced alterations in PVDF’s crystalline structure lead to diverse FTIR transmission patterns across different locations within the material. FTIR spectral peaks of PVDF, ZnO NPs, and PNC with different bond types are tabulated in Table 4.

UV-Vis absorption analysis

UV-visible absorption spectroscopy is employed to investigate the optical properties of materials. The absorption spectra were recorded within the range of 250–600 nm for ZnO NP, PVDF and PNC’s thin films, as illustrated in Fig. 6. The UV-Vis absorption spectra of PNCs and ZnO NPs reveal an absorption peak at 357 nm, confirming the presence of ZnO NPs within the PNCs. It is noteworthy that the absorption intensity increases with the incorporation of ZnO into the PVDF matrix. Whereas, pristine PVDF exhibits an absorption peak at 290 nm in the UV-Vis spectra indicating the semi-crystalline nature of PVDF [12]. This observation is consistent with the findings

Table 4 FTIR spectral peaks of PVDF, ZnO NPs, and PNC with different bond types

Wave number (cm ⁻¹)	Bond type
1700	Symmetric vibrations of C=O
1600, 1500	C=C stretch, O–H bending of the ZnO NPs
3025	Symmetric stretching of CH ₂ group
2985	Asymmetric vibrations of the CH ₂ group
1450	Fluorocarbon absorption (C–F)
1000	Fluorocarbon absorption (C–F)
613, 757, and 975	β-phase of PVDF
544	Stretching vibration modes of Zn–O–Zn

**Fig. 6** UV–Visible spectra of ZnO NPs and PNC2, PNC4, PNC6, PNC8, and PNC10 thin films

from XRD analysis, further validating the existence of ZnO NPs. The inclusion of ZnO NPs enhances the absorption of UV light in the PNCs [21].

Significantly, higher absorbance values are noted in the 300–400 nm region as the wt% of ZnO NPs is increased, indicating good interaction of ZnO NPs with PVDF chains. These results underscore the effective absorption capacity of ZnO, affirming its presence within the PVDF matrix. The absorption peaks for all PNCs in the UV region of the spectra can be attributed to the excitation of electrons from the donor level to the conduction band at these energy levels [22, 23]. Beyond, 385 nm the non-sequential intensity is observed due to variation in the thickness of thin films as depicted in Table 2. This outcome contributes to the comprehensive understanding of the UV–visible absorption characteristics in our study.

Thermo-gravimetric analysis (TGA)

The thermal stability of the PNC thin films was assessed using thermogravimetric analysis (TGA). The thermographs of pristine PVDF and PNC thin films are shown in Fig. 7. It is evident that the decomposition of pristine PVDF occurs at 424 °C, and a similar decomposition temperature range of 445–452 °C is observed for PNC thin films with varying concentrations of NPs [24, 25]. Consequently, PNCs exhibit superior thermal stability compared to pristine PVDF due to an increase in the degree of crystallinity with the addition of ZnO NPs, leading to an enhanced decomposition temperature.

The mechanism leading to chain stripping and the isolation of C–F as well as C–H bonds is responsible for the weight loss observed in the temperature range of 445–452 °C. Therefore, the addition of ZnO NPs enhances the thermal stability of the PNCs. The observed resistance of the PNCs to thermal decomposition can be attributed to the molecular interactions occurring between PVDF and the ZnO NPs [26, 27]. At lower wt%, ZnO NPs may establish stronger interactions with the PVDF matrix, influencing its thermal stability. These interactions could facilitate the initiation of decomposition processes, resulting in a quicker decrease in wt% of ZnO. The combination of PVDF and ZnO at specific wt% might create synergistic effects, impacting the overall decomposition behavior. These effects could lead to a more pronounced weight loss in the TGA profile compared to either PVDF alone or other weight percentages of PVDF–ZnO nanocomposites. This strong interaction between ZnO NPs and the PVDF matrix is also evident in the FTIR spectra and XRD patterns.

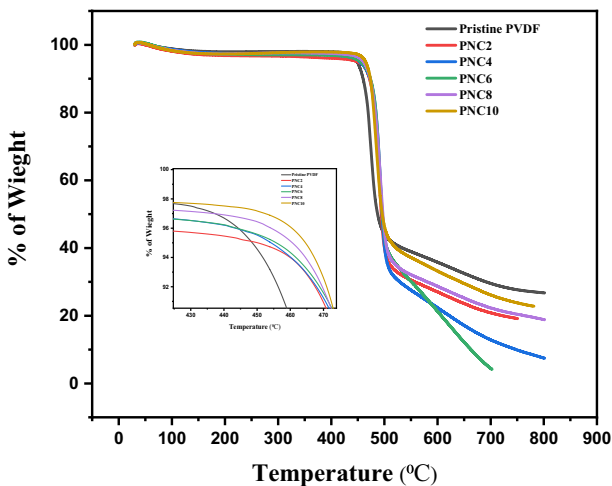


Fig. 7 Thermogram of Pristine PVDF, PNC2, PNC4, PNC6, PNC8, PNC10 thin films

Electrical properties

Dielectric properties

The dielectric constant (ϵ') and dielectric loss (ϵ'') of the PVDF and PNC thin films were calculated by using equation numbers (4) and (5), respectively:

$$\epsilon' = \frac{C_p \cdot t}{\epsilon_0 \cdot A} \quad (4)$$

$$\epsilon'' = \epsilon' \cdot \tan \delta \quad (5)$$

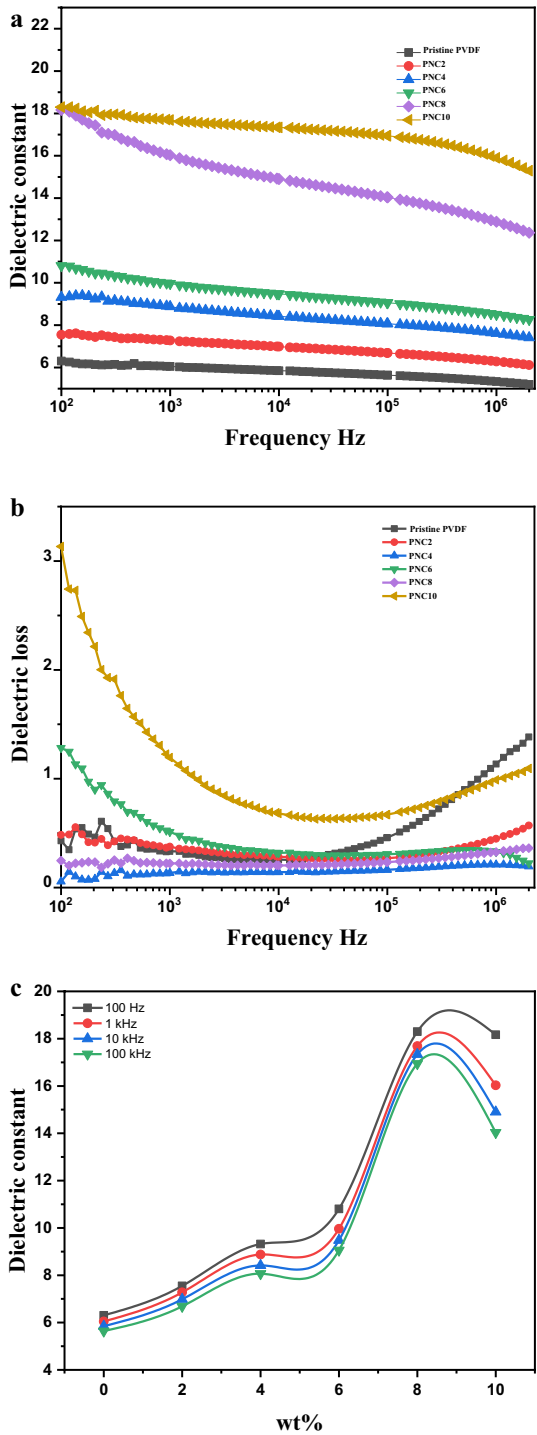
where C_p , t , ϵ_0 , A , and $\tan \delta$ are parallel capacitance (nF), thickness of the film (μm), the permittivity of free space ($8.854 \times 10^{-12} \text{ F m}^{-1}$), surface area (m^2), and tangent loss (dB), respectively.

Figure 8a depicts the variation of the ϵ' of pristine PVDF and PNC thin films with respect to the frequency over a range from 20 Hz to 2 MHz. At low frequencies, the ϵ' of pristine PVDF and PNCs is observed to be high, typically at frequency 1 kHz the ϵ' is 6.048, 7.276, 8.875, 9.963, 16.028, and 17.685 for pristine PVDF, PNC2, PNC4, PNC6, PNC8, and PNC10, respectively, primarily due to enhancement of degree of crystallinity and interfacial polarization between the ZnO NPs and PVDF interfaces, and space charge polarization. As the frequency increases, the number of charge carriers rises with the addition of ZnO NPs in the PVDF matrix, the ϵ' of PNCs decreases. This reduction is primarily attributed to interfacial polarization (depolarization), which becomes the predominant factor resisting dielectric constant at higher frequencies validating the occurrence of Maxwell–Wagner type interfacial polarization [28].

Figure 8b displays the ϵ'' of the PVDF and PNCs that decreases as the frequency increases. Higher ϵ'' is observed at lower frequencies, due to the presence of mobile charges within the PNC. Conversely, lower ϵ'' values at higher frequencies are due to the introduction of charge carriers originating from the ZnO NPs. Additionally, the influence of polarons within the PVDF polymer and charge carriers from the ZnO NPs, particularly at higher wt%, contributes to the lower ϵ'' values at higher frequencies. The polarons are quasiparticles arising from the interaction between charge carriers (electrons or holes) and the surrounding lattice or molecular structure form within the PVDF matrix of PNCs. Induced by generated charge carriers, these polarons cause localized distortions in the molecular structure, exerting a substantial impact on the electrical conductivity and charge transport properties of the material. The incorporation of ZnO NPs into the PVDF matrix enhances the ϵ' of the PNC thin films. This is because of the electrically conductive ZnO NPs introduces additional charge carriers into the PNC, reducing the distance between NPs and enhancing dipole polarization within the PNC thin films. From Fig. 8c, it is evident that as the wt% of the ZnO NPs increases, the dielectric constant also rises. Consequently, the loss tends to increase [28, 29].

PVDF contains polar side groups connected by polar bonds. When it is combined with inorganic NPs, the chemical composition of the polymer repeating units is

Fig. 8 **a** Variation of ϵ' with respect to frequency of Pristine PVDF, PNC2, PNC4, PNC6, PNC8, PNC10 thin films. **b** Variation of ϵ'' with respect to frequency of pristine PVDF, PNC2, PNC4, PNC6, PNC8, PNC10 thin films. **c** Variation of ϵ' with respect to weight % of pristine PVDF, PNC2, PNC4, PNC6, PNC8, PNC10 thin films



altered through the formation of hydrogen bonds with hydroxyl groups (-OH). These hydrogen bonds confer flexibility to the polymer chain and enhance the electrical conductivity in the PNC thin films [29].

AC conductivity

Figure 9 depicts the variation of AC conductivity of the pristine PVDF and PNC thin films with respect to frequency. It is evident that the conductivity of all PNCs increases with an increase in frequency, exhibiting a behavior similar to that of pristine PVDF. The incorporation of ZnO NPs into the PVDF matrix improves the weak links between PVDF chains and promotes coupling through grain formation. This enhancement results in improved conductivity in PNCs with wt% compared to pristine PVDF. The presence of ZnO NPs between the inter-layers of PVDF chains increases in uniform orderliness as the wt% of ZnO NPs in the composites increases, as evident with peak intensities of ZnO NPs in the XRD. This orderliness, compactness, and molecular orientation contribute to the enhancement of electrical conductivity [8, 30]

Complex impedance and complex modulus measurements

Complex impedance is utilized to analyze the electrical processes within the samples. This technique incorporates conductivity, dielectric constant, loss tangent, and the conduction mechanisms within the sample. It aids in understanding the influence of grain and grain boundaries on the electrical properties of the sample across the considered frequency range [31].

Both complex impedance and electric modulus are employed to study conduction processes in samples. These studies provide insights into the roles played by

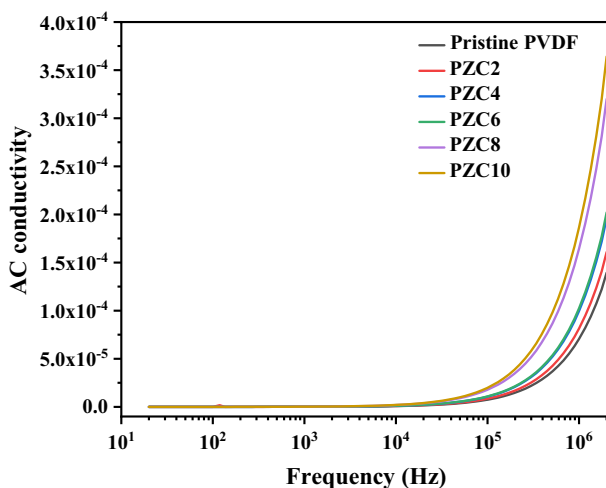


Fig. 9 Variation of AC conductivity with respect to frequency of Pristine PVDF, PNC2, PNC4, PNC6, PNC8, PNC10 thin films

resistive and capacitive elements with the smallest capacitance in an equivalent circuit, respectively. Consequently, these two analyses enable the separate examination of the effects of the polymer and filler. The real and imaginary parts of the impedance are calculated using Eq. (6) and (7) as given below:

$$Z' = Z * \cos \phi \tag{6}$$

$$Z'' = Z * \sin \phi \tag{7}$$

where $Z^* = Z' + iZ''$ is complex number, Z' (real part) and Z'' (imaginary part) of real number given by. $Z' = \frac{1}{\omega C_0} \left(\frac{\epsilon''}{\epsilon'^2 + \epsilon''^2} \right)$ and $Z'' = \frac{1}{\omega C_0} \left(\frac{\epsilon'}{\epsilon'^2 + \epsilon''^2} \right)$.

The real and imaginary parts of the electric modulus are calculated using Eq. (8) and (9).

$$M' = \omega C_0 Z' \tag{8}$$

$$M'' = \omega C_0 Z'' \tag{9}$$

where $C_0 = \frac{A\epsilon_0}{d}$, ϵ_0 —permittivity of free space, A —area of cross section, and d —thickness of the sample.

Figure 10 shows the plot of imaginary part of the impedance Z'' with frequency. Z'' reaches a maximum peak (Z''_{\max}) at a particular frequency before it decreases as the frequency increases. Notably, all the curves for the PNC thin films with different wt% of ZnO NPs converge at higher frequencies. These peaks correspond to the polarization resistance of the samples and signify a reduction in the bulk resistance of the sample. These findings align well with the results obtained for the dielectric constant as a function of the wt% of ZnO NPs with frequencies [32].

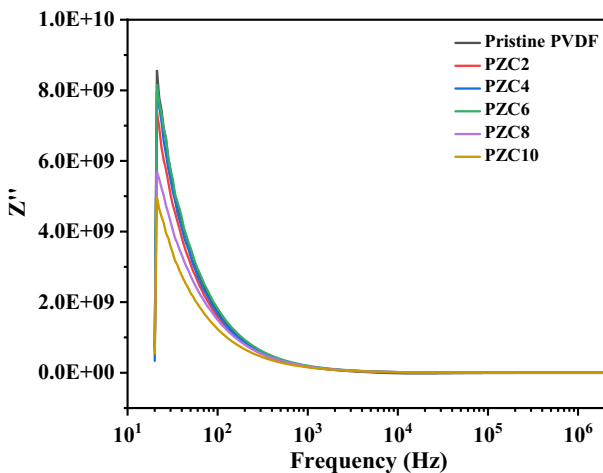


Fig. 10 Variation of imaginary part of impedance Z'' with respect to frequency of Pristine PVDF and PNC2, PNC4, PNC6, PNC8, PNC10 thin films

Figure 11a and b display the Cole–Cole plots of both pristine PVDF and the PNC thin films represented as Nyquist impedance plots. In these plots, all the films exhibit semicircles, indicating a large value for bulk resistance. Interestingly, the semi-circular arcs appear to have their centers below the real axis (Z' -axis), suggesting the presence of a non-Debye type of relaxation mechanism in the PNC thin films. To interpret and analyze such experimental data, we employ Z-view simulation

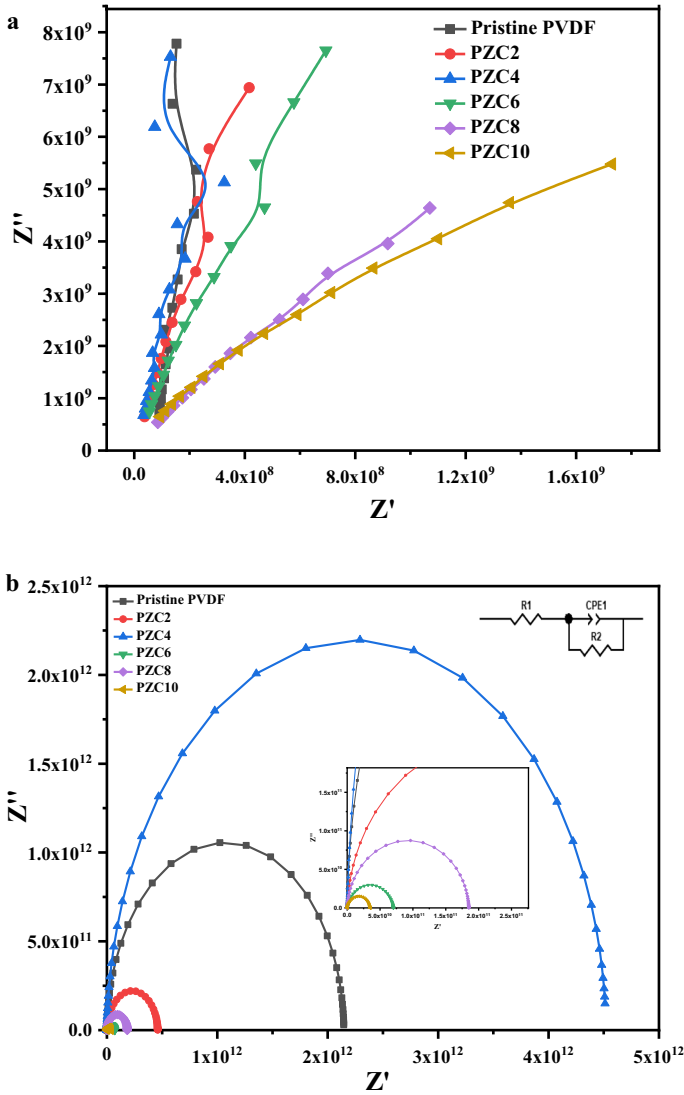


Fig. 11 a Experimental data points of Cole–Cole plot for PVDF and PNC2, PNC4, PNC6, PNC8, PNC10 thin films. b Theoretically fitted data points with equivalent electrical circuit model of Cole–Cole plot for PVDF and PNC2, PNC4, PNC6, PNC8, PNC10 thin films

software, which allows us to fit the curves by selecting a suitable equivalent circuit model, typically involving a simple resistor and capacitor (RC) circuit. This model provides a reasonable representation of the electrical properties. However, due to the non-Debye type behavior and the dispersion of capacitance, resistance, or both, an additional element called the constant phase element (CPE) needs to be introduced [31–33] for suitable fitting of the curve.

The values of the imaginary part (Z'') are higher compared to the real part (Z') of the complex impedance, confirming the high capacitive behavior of the PNC thin films. The angle of the onset curve with respect to the real part (Z') is observed to be the lowest for the PNC with 10 wt% compared to other wt% films, suggesting that it has minimal resistivity and higher conductivity.

From Fig. 11b, it is evident that, as the wt% of the ZnO NPs increases, the initial part of slope of the curve bends toward the real part (Z') axis, and there is also a shift of the center of the semicircles toward the origin. These observations indicate an increase in the conductivity of the PNC thin films as well as enhanced dipolar relaxation. The presence of semicircles in the complex impedance plane indicates that conduction occurs more within the grains rather than at the grain boundaries [34]. The non-sequential patterns are attributed to presence of grain boundaries in the composite material can create different electrical pathways, resulting in non-sequential cole–cole plots due to diverse charge transport mechanisms.

Complex electric modulus measurements provides insights into electrical transport phenomena and parameters such as carrier ions, relaxation time, conductivity, bulk properties, and the minimum capacitance present in the dielectric material under study. The real part of the modulus (M') is calculated using Eq. (8). In Fig. 12a, the variation of M' with frequency is presented. From the graph, it is evident that the values of M' are quite negligible at lower frequencies. However, as the frequency increases, M' increases for all samples. This behavior can be attributed to the presence of conduction phenomena arising from the short-range mobility of charge carriers [35].

The imaginary part of the modulus (M'') is calculated using Eq. (9), and the variation of the imaginary part of the modulus (M'') with frequency is shown in Fig. 12b. For pristine PVDF, a peak occurs relatively in the low-frequency region than PNCs, and there is a shift of the peak toward the higher-frequency region as the ZnO NPs are incorporated into the PVDF matrix. This asymmetric peak broadening indicates the spread of relaxation time with different time constants.

The relaxation peaks at higher frequencies are mainly due to the relaxation of ZnO NPs as fillers in the PNC thin films. The ZnO NPs attach to the –OH groups in the polymer, providing a faster relaxation pathway due to their small molecular size compared to the polymer. Consequently, the relaxation occurring here is of the non-Debye type. This behavior reflects the mobility of charged ions from short range to long range and the impact of grain boundary capacitance. As the frequency increases, all the curves converges trend into a single line, indicating the presence of a long-range conductivity process [32, 35]. The variability in interfacial interactions between ZnO NPs and the PVDF matrix at different frequencies could notably impact the dielectric behavior, particularly in the low-frequency range, causing discrepancies. Additionally, the influence of

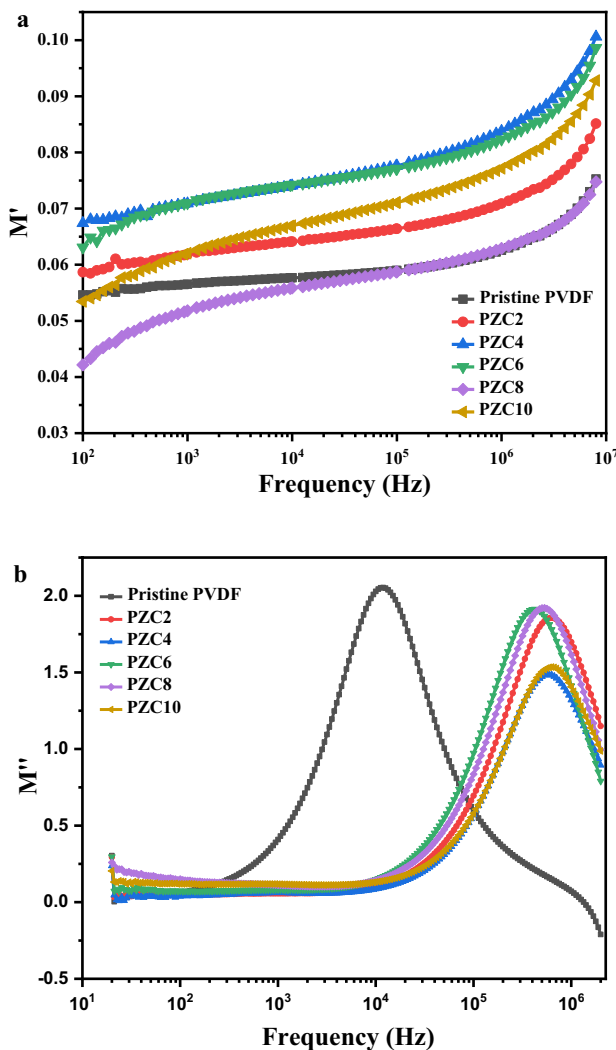


Fig. 12 a Variation of real part of electric modulus M' with respect to frequency of Pristine PVDF and PNC2, PNC4, PNC6, PNC8, PNC10 thin films. b Variation of imaginary part of electric modulus M'' with respect to frequency of Pristine PVDF and PNC2, PNC4, PNC6, PNC8, PNC10 thin films

ZnO NPs may not show a linear correlation with their wt% in the PVDF matrix at lower frequencies due to complex interactions. Furthermore, diverse relaxation mechanisms at varying frequencies might lead to differing impacts on the dielectric behavior across various wt% of ZnO NPs, contributing to non-proportional discrepancies.

Conclusion and scope of work

PVDF and PNC thin films were successfully fabricated using the solution casting method with varying wt% of ZnO NPs. Characterization studies, including XRD, FTIR, UV–Vis absorption, and TGA, confirmed the presence of β -phase PVDF with hexagonal ZnO NPs. This resulted in enhanced UV light absorption and improved thermal stability of PNCs compared to pristine PVDF. The increase in dielectric constant (ϵ'), reduction in dielectric loss (ϵ''), higher conductivity with increased ZnO NP content, and improved charge carrier mobility in the PVDF matrix were attributed to Maxwell–Wagner interfacial polarization, enhancing the polarity of the PNCs. Impedance and electrical modulus measurements revealed enhanced conductivity and a non-Debye relaxation mechanism in the thin films, indicating potential for energy storage device separators. Future work may focus on optimizing PNC film properties to improve energy storage system performance and safety.

Acknowledgements The authors are thankful to the Inter-University Accelerator Centre (IUAC), New Delhi, for extending the instrument facility under project BTR-1:68127. One of the authors, Santhoshkumar Dani acknowledges the IUAC for financial support under the project BTR-3:UFR-70320 and Arshad Ayub Hasamkal, is thankful to the Department of minorities, Govt. of Karnataka for granting fellowship.

Author contributions All authors contributed to the study conception and design. AAH and SD prepared samples and analyzed data; while, Bibi Raza Khanam performed characterization. RM and JAV conducted formal analysis, methodology, review, and editing, and provided validation. UVK supervised, conceptualized the investigation, conducted formal analysis, and participated in writing, review, and editing. All authors approved the final manuscript.

Funding The authors declare no competing financial interest.

Data availability The raw or processed data required to replicate these findings in the current study are available from the corresponding author upon reasonable request.

Declarations

Conflict of interests The authors have no relevant financial or non-financial interests that could influence the work reported in this paper.

References

1. Abdah MAAM et al (2021) Synthesis and electrochemical characterizations of poly (3, 4-ethylenedioxythiophene)/manganese oxide coated on porous carbon nanofibers as a potential anode for lithium-ion batteries. *Energy Rep* 7:8677–8687. <https://doi.org/10.1016/j.egy.2021.10.110>
2. Alidoost M et al (2022) Micro-mesoporous carbons from cyclodextrin nanosponges enabling high-capacity silicon anodes and sulfur cathodes for lithiated Si-S batteries. *Chem—A Eur J* 28(6):e202104201. <https://doi.org/10.1002/chem.202104201>
3. Wu H et al (2022) Polymer-/ceramic-based dielectric composites for energy storage and conversion. *Energy Environ Mater* 5(2):486–514. <https://doi.org/10.1002/eeem2.12237>
4. Chen H et al (2018) Exploring chemical, mechanical, and electrical functionalities of binders for advanced energy-storage devices. *Chem Rev* 118(18):8936–8982. <https://doi.org/10.1021/acs.chemrev.8b00241>

5. Dyartanti ER et al (2018) Ionic conductivity and cycling stability improvement of PVdF/nano-clay using PVP as polymer electrolyte membranes for LiFePO₄ batteries. *Membranes* 8(3):36. <https://doi.org/10.3390/membranes8030036>
6. Dyartanti ER et al (2018) Nanocomposite polymer electrolytes in PVDF/ZnO membranes modified with PVP for LiFePO₄ batteries. *Evergreen*. <https://doi.org/10.5109/1936213>
7. Hari MA et al (2021) Effect of nanoparticle size on the piezoelectric properties of PVDF based nanocomposite thin films. *Mater Today: Proc* 46:5781–5784. <https://doi.org/10.1016/j.matpr.2021.02.715>
8. Tan KS et al (2014) Pyroelectricity enhancement of PVDF nanocomposite thin films doped with ZnO nanoparticles. *Smart Mater Struct* 23(12):125006. <https://doi.org/10.1088/0964-1726/23/12/125006>
9. Lu H et al (2017) Improved dielectric strength and loss tangent by interface modification in PI@BCZT/PVDF nano-composite films with high permittivity. *J Mater Sci: Mater Electron* 28:13360–13370. <https://doi.org/10.1007/s10854-017-7173-2>
10. Kulkarni S, Patil AH, Mathad SN, Khadke UV (2021) Dielectric spectroscopy of ferroelectric cross-bred PVDF-ZnO polymer composite thin films. *J Nano-Electron Phys.* 13(4):04014. [https://doi.org/10.21272/jnep.13\(4\).04014](https://doi.org/10.21272/jnep.13(4).04014)
11. Martins P, Lopes AC, Lanceros-Mendez S (2014) Electroactive phases of poly (vinylidene fluoride): determination, processing and applications. *Prog Polym Sci* 39(4):683–706
12. Dani S et al (2022) The electromagnetic interference shielding effectiveness and dielectric response of PVDF-nTiO₂ nanocomposites thin films. *Trends Sci* 19(21):3046–3046. <https://doi.org/10.48048/tis.2022.3046>
13. Arshad AH et al (2023) Dielectric spectroscopy of ferroelectric crossbred PVDF-TiO₂ polymer composite thin films. *J Sci Res* 15:1. <https://doi.org/10.3329/jsr.v15i1.60132>
14. Devi PI, Ramachandran K (2011) Dielectric studies on hybridised PVDF-ZnO nanocomposites. *J Exp Nanosci* 6(3):281–293. <https://doi.org/10.1080/17458080.2010.497947>
15. Rajeh A, Ragab HM, Abutalib MM (2020) Co doped ZnO reinforced PEMA/PMMA composite: structural, thermal, dielectric and electrical properties for electrochemical applications. *J Mol Struct* 1217:128447. <https://doi.org/10.1016/j.molstruc.2020.128447>
16. Thakur P et al (2018) Superior performances of in situ synthesized ZnO/PVDF thin film based self-poled piezoelectric nanogenerator and self-charged photo-power bank with high durability. *Nano Energy* 44:456–467. <https://doi.org/10.1016/j.nanoen.2017.11.065>
17. Wang G et al (2008) Fabrication of radial ZnO nanowire clusters and radial ZnO/PVDF composites with enhanced dielectric properties. *Adv Func Mater* 18(17):2584–2592. <https://doi.org/10.1002/adfm.200800109>
18. Archana S (2017) AC conductivity and dielectric behavior of poly (o-phenylenediamine)/ZnO nanocomposites. *IJAR* 3(4):661–667. <https://doi.org/10.14419/ijac.v5i1.7437>
19. Mohammed MI (2021) Dielectric dispersion and relaxations in (PMMA/PVDF)/ZnO nanocomposites. *Polymer Bull.* <https://doi.org/10.1007/s00289-021-03606-z>
20. Pervaiz S et al (2021) Study of structural, optical and dielectric properties of ZnO/PVDF-based flexible sheets. *J Polym Res* 28:1–13. <https://doi.org/10.1007/s10965-021-02640-9>
21. Indolia AP, Gaur MS (2013) Optical properties of solution grown PVDF-ZnO nanocomposite thin films. *J Polym Res* 20:1–8. <https://doi.org/10.1007/s10965-012-0043-y>
22. Shanshool HM et al (2016) Investigation of energy band gap in polymer/ZnO nanocomposites. *J Mater Sci: Mater Electron* 27:9804–9811. <https://doi.org/10.1007/s10854-016-5046-8>
23. Arularasu MV et al (2020) PVDF/ZnO hybrid nanocomposite applied as a resistive humidity sensor. *Surf Interfaces* 21:100780. <https://doi.org/10.1016/j.surfin.2020.100780>
24. Jaleh B, Jabbari A (2014) Evaluation of reduced graphene oxide/ZnO effect on properties of PVDF nanocomposite films. *Appl Surf Sci* 320:339–347. <https://doi.org/10.1016/j.apsusc.2014.09.030>
25. Nguyen VS et al (2013) Influence of cluster size and surface functionalization of ZnO nanoparticles on the morphology, thermomechanical and piezoelectric properties of P(VDF-TrFE) nanocomposite films. *Appl Surf Sci* 279:204–211. <https://doi.org/10.1016/j.apsusc.2013.04.070>
26. Joshi S et al (2022) Improved electrical signal of non-poled 3d printed zinc oxide-polyvinylidene fluoride nanocomposites. *Polymers* 14(20):4312. <https://doi.org/10.3390/polym14204312>
27. Sathiyaraju M, Ramesh T (2019) Nanomechanical, mechanical responses and characterization of piezoelectric nanoparticle-modified electrospun PVDF nanofibrous films. *Arab J Sci Eng* 44:5697–5709. <https://doi.org/10.1007/s13369-018-03694-6>

28. Ponnamma D et al (2019) Synthesis, optimization and applications of ZnO/polymer nanocomposites. *Mater Sci Eng, C* 98:1210–1240. <https://doi.org/10.1016/j.msec.2019.01.081>
29. Parangusan H et al (2018) Stretchable electrospun PVDF-HFP/Co-ZnO nanofibers as piezoelectric nanogenerators. *Sci Rep* 8(1):754. <https://doi.org/10.1038/s41598-017-19082-3>
30. Bhunia R et al (2016) Flexible nano-ZnO/polyvinylidenedifluoride piezoelectric composite films as energy harvester. *Appl Phys A* 122:1–13. <https://doi.org/10.1007/s00339-016-0161-1>
31. Nayak A et al (2019) Impedance spectroscopy of Pb0.8La0.2Fe0.1Cr0.1Ti0.8O3. In: IOP conference series: materials science and engineering, vol 577, no. 1. IOP Publishing. <https://doi.org/10.1088/1757-899X/577/1/012048>
32. Sahoo PS et al (2010) Impedance spectroscopy of Ba₃Sr₂DyTi₃V₇O₃₀ ceramic. *Bull Mater Sci* 33:129–134. <https://doi.org/10.1007/s12034-010-0018-8>
33. Hemalatha KS, Rukmani K (2017) Concentration dependent dielectric, AC conductivity and sensing study of ZnO-polyvinyl alcohol nanocomposite films. *Int J Nanotechnol* 14(9–11):961–974. <https://doi.org/10.1504/IJNT.2017.086778>
34. BelalHossen M, AktherHossain AKM (2015) Complex impedance and electric modulus studies of magnetic ceramic Ni_{0.27}Cu_{0.10}Zn_{0.63}Fe₂O₄. *J Adv Ceram* 4:217–225. <https://doi.org/10.1007/s40145-015-0152-2>
35. Ali MA et al (2015) Structural properties, impedance spectroscopy and dielectric spin relaxation of Ni-Zn ferrite synthesized by double sintering technique. *J Sci Res.* <https://doi.org/10.3329/jsr.v7i3.23358>

Publisher's Note Springer Nature remains neutral with regard to jurisdictional claims in published maps and institutional affiliations.

Springer Nature or its licensor (e.g. a society or other partner) holds exclusive rights to this article under a publishing agreement with the author(s) or other rightsholder(s); author self-archiving of the accepted manuscript version of this article is solely governed by the terms of such publishing agreement and applicable law.